

Non-Gaussian and anisotropic fluctuations mediate the progression of global cellular order: a data-driven study

Mengyang Gu,^{1,*} Xinyi Fang,¹ and Yimin Luo^{2,*}

¹*Department of Statistics and Applied Probability,
University of California, Santa Barbara, Santa Barbara, CA 93106, USA*

²*Department of Mechanical Engineering and Materials Science, Yale University, New Haven, CT 06511, USA*
(Dated: March 8, 2023)

The dynamics of cellular pattern formation are crucial for understanding embryonic development and tissue morphogenesis. Recent studies have shown that human dermal fibroblasts cultured on liquid crystal elastomers can exhibit an increase in orientational alignment over time, accompanied by cell proliferation, under the influence of the weak guidance of a molecularly aligned substrate. However, a comprehensive understanding of how this order arises remains largely unknown. This knowledge gap may be attributed, in part, to a scarcity of mechanistic models that can capture the temporal progression of the complex nonequilibrium dynamics during the cellular alignment process. To fill in this gap, we develop a hybrid procedure that utilizes statistical learning approaches to select individual-level features for extending the state-of-art physics models. The maximum likelihood estimator of the model was derived and implemented in computationally scalable algorithms for model calibration and simulation. By including these features, such as the non-Gaussian, anisotropic fluctuations, and limiting alignment interaction only to neighboring cells with the same velocity direction, this model is able to reproduce system-level parameters: the temporal progression of the velocity orientational order parameters and the variability of velocity vectors. Unlike other data-driven approaches, we do not rely on a loss function to tune model parameters to match these system-level characteristics. Furthermore, we develop a computational toolbox for automating model construction and calibration that can be applied to other systems of active matter.

I. INTRODUCTION

Active matter refers to systems composed of many individual agents that interact with each other and consume energy from their surroundings or an internal source to generate complex, global behaviors [1–3]. It encompasses a wide range of biological systems, such as flocks of birds, schools of fish, groups of humans, herds of sheep, monolayers of cells, colonies of bacteria, and others, all exhibiting intriguing out-of-equilibrium phenomena. The dynamics of active matter, which we term “active dynamics”, is the key to describing the collective, spatiotemporal self-organizations of these systems, which come forth from interactions and decision-making at the individual agent level.

Disorder-to-order transitions in biological tissues, characterized by the emergence of patterns, are a common feature of cellular systems. These transitions have been compared to phases of matter, such as disordered gas and amorphous solids [4, 5]. They underlie many developmental processes [6], and are implicated in cancer invasion [7]. The resulting patterns impart tissue with form, function, and integrity, as seen in the basket-weave-like pattern of the dermis that serves as a shield for the deeper layers [8, 9], the generation of forces in blood vessels [10, 11], and the coordination of cell fates during embryonic development [12].

The mechanisms behind these cellular transitions are not well understood, but traditionally, collective behav-

iors are thought to be regulated by cell chemosensing [13], and upstream biochemical signaling pathways [14]. While biochemical regulations are on-demand and short-lived, physical guidance ensures the generation of cell phenotypes and long-term maintenance of tissue structures [15]. More recently, simple 2D transitions of such nature have been realized through *in vitro* experiments [16–19], by subjecting a cell monolayer to an external guiding field, such as a well-aligned molecular field [20], which can lead cells to collectively orient along a predetermined axis in a density-dependent manner.

Modeling the spontaneous alignment of particles in active matter systems has been the subject of numerous studies [21–26]. The two main approaches in modeling are either by constructing mechanistic models by physical laws, or by applying data-driven methods to extract information from observations to construct models [27, 28]. In data-driven methods, regression techniques, for instance, are widely applied to estimate linear coefficients of a set of additive basis [29–31], or particle interaction functions by neural networks [32] or Gaussian processes [33]. Despite the prevalence of the disorder-to-order transition observed in experiments, capturing the temporal progression of dynamic quantities in active matter systems, such as the orientational order parameter and variability of velocity, remains a challenging task due to a few reasons.

First of all, active matter systems intrinsically contain large fluctuations, yet portraying such a term has rarely been the focus of model construction. Gaussian distributions of fluctuation, for instance, are often assumed for modeling the progression of the velocity in construct-

* Corres. authors: mengyang@pstat.ucsb.edu; yimin.luo@yale.edu

ing mechanistic models [34, 35]. In a data-driven approach, the model is usually optimized by minimizing a loss function. One common choice of the loss function is the sum of squared errors, and minimizing it is equivalent to finding the maximum likelihood estimator, under the assumption of having independent Gaussian noises with homogeneous variances. However, we find velocity distributions from our experiments significantly deviate from Gaussian. In fact, even though models assuming Gaussian distribution of the velocity fluctuation can fit the magnitude of temporally dependent velocity, they cannot capture the progression of orientational order parameters and velocity fluctuation at the distribution level. Non-Gaussian distributions of displacements have been widely observed in biological systems, such as particles absorbed on lipid bilayers [36], immersed in entangled actin solutions [36] and in a bath of swimming algal cells [37], liposomes in active actin solutions [38], and receptors on living cell membranes [39]. Despite extensive observations, fluctuation distributions have not been widely incorporated in simulation models, partly due to the challenges in obtaining efficient estimators, such as the maximum likelihood estimator, for these models.

Secondly, in principle, having a large number of observations containing thousands of particle trajectories over hundreds of time points can help offset the uncertainty of estimation due to large fluctuations of the active particles. Nonetheless, calibrating the simulation model with such a large number of observations is a non-trivial task. Hence, there is a need for robust and computationally scalable algorithms to extract features from a large number of observations. Furthermore, though an efficient grid-based technique [40] is known for reducing the complexity of simulation with local cellular interactions from $\mathcal{O}(n_t^2)$ to $\mathcal{O}(n_t)$, where n_t is the number of cells at time t , it is less known how to adapt it for the purpose of accelerating parameter estimation from a large number of observations.

This work aims to address these issues by introducing an efficient workflow to automate model construction, promoting convergence between simulation and experiment. We take a hybrid approach that integrates physical models and statistical learning approaches: First, we start from a conventional form of the physical models (e.g. the Vicsek model [21, 41]). Second, we apply statistical tests for feature selections. Then, these features are utilized to construct a data-generative model, instead of minimizing a loss function as usually adopted in other data-driven discovery approaches. The data generative model provides a better physical interpretation of the estimated quantities, and more importantly, the uncertainty of the estimation can also be quantified. We develop an automated feature selection and estimation approach, which is applied to learning physical quantities from live microscopy of fibroblasts moving on liquid-crystalline substrates, to discover a variety of new features. Simulation models constructed with these new features can reproduce the progression of system properties,

such as orientational order parameters and velocity distributions, whereas models missing any of these features do not match experimental findings.

To summarize, the contributions of this work are two-fold. Our first contribution is to discover four new features from video microscopy of cellular movement experiments on liquid-crystalline substrates using statistical tests, which can be classified into two groups. First, we found the velocity of the cells is anisotropic and has more probability mass around zero and heavy tails than a Gaussian distribution, motivating the use of a Laplace distribution or generalized Gaussian distribution of fluctuation. Though the Laplace distribution was used to fit the probability distribution of the displacements in different experiments [36, 38, 42], its effect on capturing the progression of the orientational order parameter in simulations has seldom been demonstrated. The second group of discovery concerns cellular interactions. While the velocity of a cell can be largely explained by the velocities of neighboring cells, our findings indicate that cells are not perfectly aligned with the average of their neighbors, as is the case in the classic Vicsek model [21]; Instead, effects from the previous step shrink towards zero, likely due to a frictional force term in the Langevin equation [43]. Additionally, we discovered that cells traveling in the opposite direction may be excluded from the neighboring set, leading to improved predictions of the velocity at the subsequent time point. This likely arises from the nematic nature of cell-cell interactions [44], where opposing cells can simply glide past each other without influencing each other's velocity.

Our second contribution involves the development of a computational toolbox that enables visualization, hypothesis testing, scalable parameter estimation, and simulation of active dynamics. Fig. 1 illustrates an instance of a particle-based analysis module within our toolbox. Other techniques that do not require particle-tracking algorithms, such as differential dynamic microscopy [45, 46], can also be utilized to extract ensemble properties like mean squared displacements. In Fig. 1(c), we present a plot showing the correlation between cellular velocity and the mean velocity of neighboring cells in the previous time point. The slopes of the best-fit lines (red solid curve) are smaller than 1 for both x and y directions. To determine if this result applies to all time points, we plot the fitted weight parameters (equivalent to the slope of the fit in Fig. 1(c)) over time and calculate the 95% confidence interval, which is represented by the shaded area in Fig. 1(d). The upper bounds of the 95% confidence intervals are substantially smaller than 1, indicating that the weight parameters must be included in the simulation model. All the identified features are included in the simulation model, and a maximum likelihood estimator is derived for efficient parameter estimation (Appendices A & B). For both parameter estimation and simulation, we employ a grid-based approach by storing the particles in a coarse-grained grid (Fig. 1(e)). Our tool can analyze cell alignment in a high-

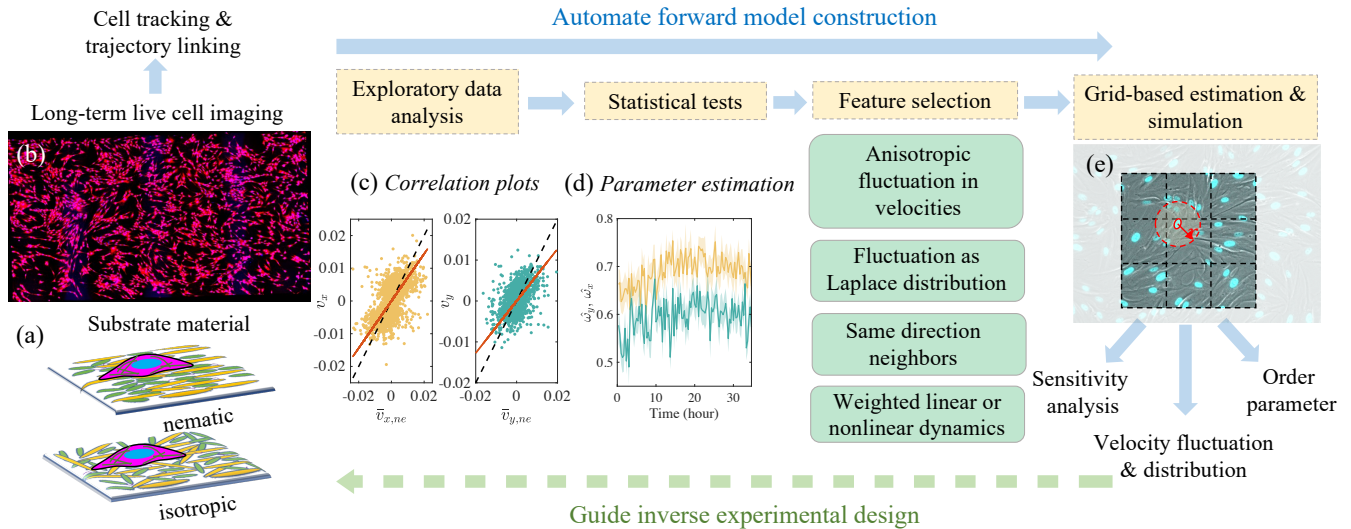


FIG. 1. (a) Schematics of the two types of substrates (isotropic and nematic) tested in this study. (b) A stitched view of a snapshot of long-term cell imaging where cell cytoplasm is labeled in red. (c) Correlation plots in exploratory data analysis indicate the slope of the fit (red solid lines) is smaller than 1 (black dashed lines). (d) Parameters estimation of the slope parameters and 95% confidence interval (shaded area). The statistical tests yield 4 potential features (green blocks). (e) Using the grid-based system to search for the neighbors. In order to find the neighbor of the target cell i (circled in red), a radius of r will be searched. The computational procedure is simplified by only searching through neighboring squares connected to the square cell i is located in.

throughput manner: With a typical microscopy video of $n = 2500$ cells and $T = 100$ time frames, the time it takes to perform feature selection, parameter estimation, and simulation of dynamics with particle interactions, is less than 30 seconds on a desktop computer. This provides almost immediate feedback that can be used to inversely guide the design of the experiment.

II. FEATURE SELECTION FROM EXPERIMENTAL RESULTS

We begin by discussing experimental methods for live cell imaging and the process of extracting trajectories from cells cultured on different liquid-crystalline substrates. We then conduct exploratory data analysis and statistical tests to identify significant features from the experimental data. These features are used as building blocks to extend a baseline model. Lastly, we perform simulations to validate our findings in Section III.

A. Experimental setting: in vitro cell alignment experiment

The experimental data were derived from [20], where liquid crystal elastomer (LCE) substrates were fabricated with a mixture of reactive monomers RM82 and RM23 (SYNTHON Chemicals GmbH & Co.) in a 1:1 molar ratio with the molecular field having either isotropic or nematic (uniform along the x -direction) configurations.

Human dermal fibroblasts (hdFs, American Type Culture Collection) were seeded onto the substrates at $\sim 50 \text{ mm}^{-2}$, and grown to desired densities. Prior to imaging, the nuclei were stained with Hoechst 33342 (ThermoFisher). Cells are maintained at 37°C , $5\% \text{ CO}_2$ and imaged every 20 min for about 36 hours. Tens of images were taken at every time point and stitched together to construct an image on the order of mm^2 in area. LCE nematic substrates impose a molecular direction to guide hdF growth. During the experiment, cell density ρ grows from roughly 350 to 400 mm^{-2} . With an increase in cell density, the monolayer undergoes a disorder-to-order transition. To obtain the trajectories as inputs, we fit an ellipse to the nuclei and track particle trajectories using a standard tool, such as ImageJ [47]. On the nematic substrate, cells develop a long-range order along the x -direction, the same direction as the molecular orientation in the aligned substrate, but not on isotropic substrates.

From the experiment, we extract the 2D position vector $\mathbf{s}_i(t) = (s_{i,x}(t), s_{i,y}(t))^T$ and velocity vector $\mathbf{v}_i(t) = (v_{i,x}(t), v_{i,y}(t))^T$ of cell i , at time frame t , for $i = 1, \dots, n_t$, with n_t being the number of cells on time frame t , for $t = 1, \dots, T$. The goal is to construct an interpretable model and constrain the model by data, for reproducing the temporally dependent variability of the velocity and orientational order parameter. We plot the standard deviation of the velocity at x and y directions at each time frame in Fig. 2(a). Since the nucleus does not distinguish between the head and tail, its order is apolar, we cannot apply the polar order parameter to quantify the system [48]. Instead, we first transform ve-

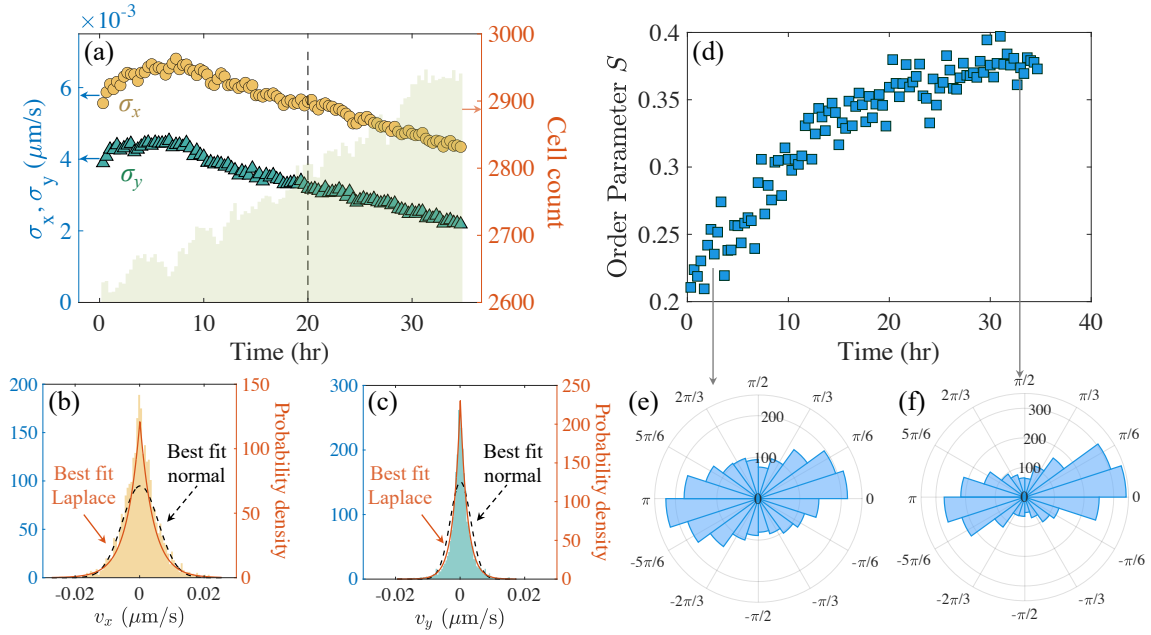


FIG. 2. Parameters estimated from the data set. (a) The standard deviation of the cell velocities is shown in yellow circles and green triangles. The light-colored histogram denotes the cell number count (b-c). The velocity distribution at a representative time = 20 hours. The dashed black lines denote the best fit normal distribution. The solid orange lines denote the best fit Laplace distribution. (d) The blue squares denote the polar order parameter, and the polar histograms of the velocity angle at two different time points are plotted in (e-f).

locity angle of the particle i at time frame t , denoted by $\theta_i(t) = \arctan(v_{i,y}(t)/v_{i,x}(t))$, to $[0, \pi]$ by letting:

$$\tilde{\theta}_i(t) = \begin{cases} \theta_i(t) + \pi & \text{if } \theta_i(t) < 0, \\ \theta_i(t) & \text{if } \theta_i(t) \geq 0. \end{cases} \quad (1)$$

The orientational order parameter at time t is an ensemble of transformed velocity angles amongst all cells: $S(t) = \langle \cos(2\tilde{\theta}_i(t)) \rangle_i$. This way, anti-parallelly traveling cell pairs ($\theta_i = \theta_j + \pi$) have the same contribution to orientational order parameters. In Fig. 2(d), we show that the orientational order parameter $S(t)$ increases with time. The distributions of the velocity angles at two different time points are plotted in Fig. 2(e) and (f), showing that over time the velocity distribution becomes more parallel along x -direction.

To account for observed migrational patterns, we start by identifying unexpected deviations of the magnitude and distributions from the classical Viscek Model. Exploratory data analysis (EDA) [49] is a useful step to visualize patterns from complex experimental data before performing statistical tests and modeling. Here, we first perform EDA on various aspects of the data, followed by statistical tests and estimation to identify features to include in the modeling. The main text focuses on the analysis of an experiment where cells initially cover roughly 50% of the substrates. During the experiment, the order parameter increases rapidly with cell proliferation. We present results on the analysis of two additional experi-

ments at different cell densities or on isotropic substrates in Appendix C.

B. Permutation F-test on variances of the velocities

To test whether the variances of the velocities along x and y directions are the same at all time frames, we first compute the sample standard deviation of the velocity vector at x and y coordinates: $\hat{\sigma}_x^2(t) = \sum_{i=1}^{n_t} (v_{i,x}(t) - \bar{v}_x(t))^2 / (n_t - 1)$ and $\hat{\sigma}_y^2(t) = \sum_{i=1}^{n_t} (v_{i,y}(t) - \bar{v}_y(t))^2 / (n_t - 1)$, where $\bar{v}_x(t)$ and $\bar{v}_y(t)$ are the mean of the velocity at time t computed from an ensemble of all cells in the system, respectively, and both are close to zero. As shown in Fig. 2(a), we found that the standard deviation of the velocity along the x coordinate is always larger compared to that along y . The larger magnitude of cellular velocity along the x coordinate is induced by the liquid-crystalline substrate, which is molecularly aligned along with the x direction in this experiment. As the velocity magnitudes along x and y directions become more unequal over time, the orientational order parameter increases (Fig. 2(d)).

Is the observed difference between $\sigma_x(t)$ and $\sigma_y(t)$ due to signal or noise? Typically, testing the equality of the variance is performed using the F-test assuming both populations are normally distributed. For any given time frame, one first computes the F statistics $F(t) = \hat{\sigma}_x^2(t) / \hat{\sigma}_y^2(t)$. When the null hypothesis ($\sigma_x^2(t) = \sigma_y^2(t)$) is true, the p-value of the test statistics is distributed as

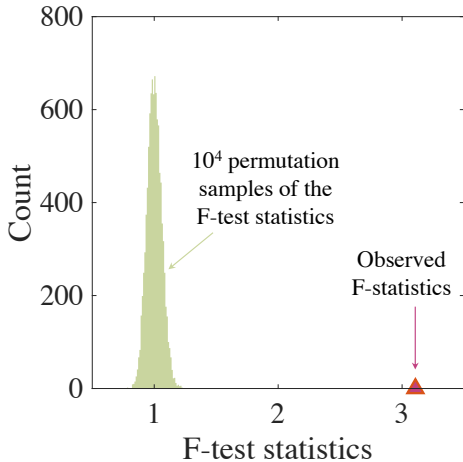


FIG. 3. A permutation F-test shows that the noise along x and y directions are indeed unequal at time =20 hrs.

the F distribution $F(n_t - 1, n_t - 1)$. However, as we will see later, velocity distributions do not follow a normal (Gaussian) distribution, while the F-test is sensitive to the normality assumption [50].

Here we circumvent the normality assumption by running a permutation F-test. The permutation test is a general nonparametric test that is insensitive to the distributional assumption. At each time t , we first combine the velocities at x and y directions in a long vector and then randomly assign the values into two groups of equal size to form a permuted sample. We repeat this step B times to collect B permuted samples: $\mathbf{v}_x^{(b)}(t) = [v_{1,x}^{(b)}(t), \dots, v_{n_t,x}^{(b)}(t)]$ and $\mathbf{v}_y^{(b)}(t) = [v_{1,y}^{(b)}(t), \dots, v_{n_t,y}^{(b)}(t)]$ for $b = 1, \dots, B$. Then we compute the permuted F-test statistics $F^{(b)}(t) = \hat{\sigma}_{b,x}^2(t)/\hat{\sigma}_{b,y}^2(t)$, where $\hat{\sigma}_{b,x}^2(t)$ and $\hat{\sigma}_{b,y}^2(t)$ denote the sample variances of the velocity for x and y directions, respectively, from the permuted sample b . The p-value is twice the minimum of the probabilities $\Pr(F^{(b)}(t) > F(t))$ and $\Pr(F^{(b)}(t) < F(t))$, which can be computed empirically using the permuted samples.

Fig. 3 shows that the distribution of the F-test statistics of the permuted samples and the observed F-test statistics for velocity observations at time equal to 20 hours, and the p-value is smaller than 10^{-4} , indicating that the variance of the velocity along x and y directions are unequal at this time frame. We perform the permutation F-test for each of the time points and the p-value for each of the tests is smaller than 10^{-4} , meaning that the variances $\sigma_x^2(t) \neq \sigma_y^2(t)$ for all time points. Thus, cellular movements are anisotropic when cells are grown on a molecularly aligned substrate.

C. Shapiro–Wilk test for normality of velocity distribution

While at first glance cell motility bears much resemblance to passive, freely diffusing particles, our study reveals that velocity distributions in our system deviate from the Gaussian distribution typically observed for passive particles in a homogeneous environment. To illustrate that, we plot the probability density function of velocity distributions at a representative time (Fig. 2(b) and (c)). Both velocity distributions along x and y have spiky modes and heavy tails, which cannot be captured by the best-fit Gaussian distribution (Fig. 2, black dashed curves), for which the mean and standard deviation are specified as the sample mean and sample standard deviation, respectively. The shape of the probability density distribution suggests the use of the Laplace distribution (Fig. 2(b) and (c), orange solid curves), which fits the velocity distributions reasonably well.

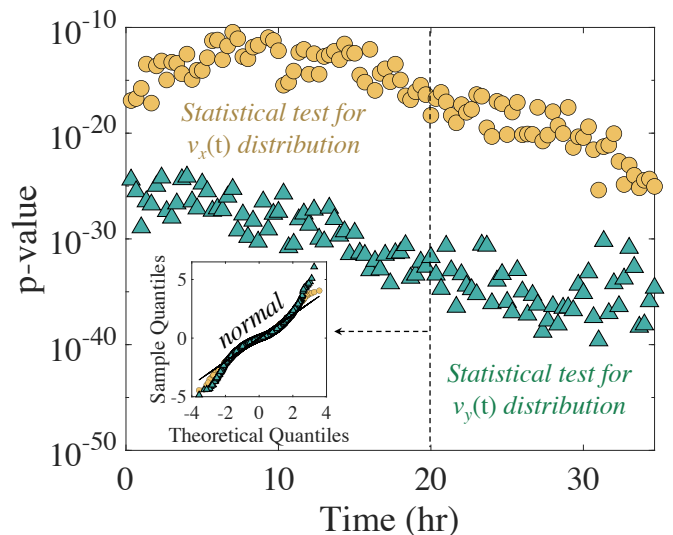


FIG. 4. Shapiro–Wilk test for normality. The figure shows the p-value of individual frames, which is a statistical measurement applied to validate whether or not the observed data follows a normal distribution. A small p-value indicates statistical significance. The inset shows a representative quantile-quantile (QQ) plot at time = 20 hours to compare the sample quantiles of normalized velocity with the theoretical quantiles from the standard normal distribution. The black curve indicates the linear curve with slope 1 (normal).

To test whether the velocity distribution follows the normal distribution at each time frame, we compute p-values of the Shapiro–Wilk test for normality [51], plotted in Fig. 4. The p-values are all extremely small, indicating the velocity distribution at any time frame substantially deviates from Gaussian. Furthermore, we plot the sample quantile-theoretical quantile from a normal distribution (QQ-plot) of the velocities along both directions at 20 hours, both of which deviate from theoretical quantiles, shown as the black line in the inset. The p-values get

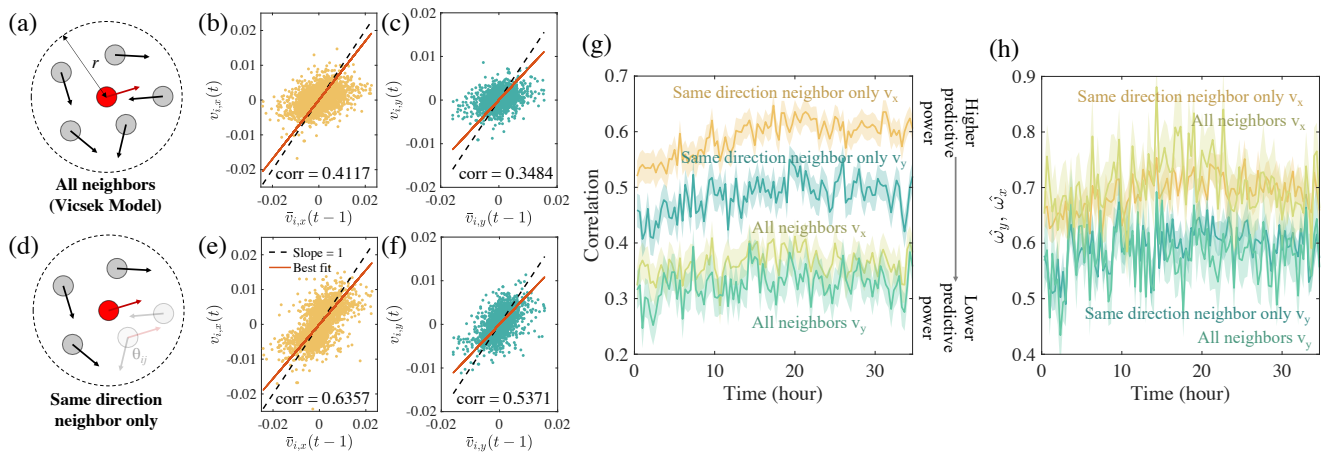


FIG. 5. Effects of accounting for different neighbor ensembles. The top row (a-c) shows parameters and correlation plots using the neighbor ensemble of the classical Vicsek Model for time = 20 hours. The bottom row (d-f) shows the scenario where only cells traveling in the same direction are considered. Panel (b), (c), (e), and (f) show the correlation between the cell at t versus the mean of the velocity of its neighbors at $t - 1$. (g) Correlations between velocity $v_{i,x}(t)$, $v_{i,y}(t)$ of any cell i and mean velocity of the neighboring cells from the previous step $\bar{v}_{i,x}(t - 1)$, $\bar{v}_{i,y}(t - 1)$, where the 95% confidence intervals, shown in faded shades, are computed based on Fisher transformation of correlation coefficients. Two scenarios are shown, either by including all neighbors (bottom 2 curves), or only the same direction neighbors (top 2 curves). (h) The estimated weights, equivalent to the fitted slopes, $\hat{\omega}_x(t)$, $\hat{\omega}_y(t)$ from these two scenarios and their confidence intervals are plotted.

smaller at later time frames when the system approaches jamming, as the network effects are larger. Furthermore, the p-values for velocities along y -direction are smaller than those from the x -direction, indicating that the deviation from normality is also bigger, signaling more confinement along y -direction.

D. Neighboring feature construction for cellular interaction

Next, we discuss the contribution of the neighbor ensemble to cell alignment. For any cell, the conventional choice of the neighboring set is to include all cells within a radius distance (as shown in Fig. 5(a)). Evidence of cell intercalation, where cells squeeze past their neighbors and they exchange positions, is increasingly found in recent studies [52, 53]. When antiparallely aligned cells move past each other, they minimally impact each other's velocity. This motivates us to investigate a neighboring set that excludes the cells with opposite velocity, as shown in Fig. 5(d). To compare these two approaches of accounting for the neighbors, in Fig. 5(b), we plot the cellular velocity of each particle $v_{i,x}(t)$ at time = 20 hours versus the mean velocity of neighboring cells at the previous time frame at x coordinate, while in Fig. 5(e) the same quantities are computed when the cells with opposite direction are excluded from the neighboring data set. It is not surprising that both approaches yield a relatively high 1-step forecast accuracy, since individual cells tend to migrate with a persistent velocity [54], and the neighboring set in the previous step includes the cell itself.

The correlation in Fig. 5(e) is around 0.64, which is substantially higher than the correlation of 0.41 in Fig. 5(b), indicating excluding the particles from the neighbors substantially improves the 1-step predictive accuracy. The same conclusion holds for velocity updates along the y coordinate, shown in Fig. 5(c) and (f). Furthermore, by evaluating the 1-step correlation over all time points (Fig. 5(g)), we find that the method including only same-direction neighbors substantially outperforms the one including all of the neighbors, as in the Vicsek Model. These results indicate that the hdF cells in our experiment appear to distinguish between head and tail polarities [55], despite extensive analogy that has been drawn between weakly interacting fibroblasts and active nematics [44, 56],

E. Reduced magnitude of local alignment

Unlike [57], we do not normalize the velocity to keep the velocity magnitude to be the same, as the velocities can also change due to an increase in cell density. Fig. 5(e) and (f) indicate that the velocity of the cell i at time t may be modeled by the mean of the velocity of the neighboring cells at time $t - 1$, that is, $\mathbb{E}[v_{i,x}(t)] = w_x(t)\bar{v}_{i,x}(t - 1)$ and $\mathbb{E}[v_{i,y}(t)] = w_y(t)\bar{v}_{i,y}(t - 1)$, where $\bar{v}_{i,x}(t - 1)$ and $\bar{v}_{i,y}(t - 1)$ are the mean of the velocity of the neighboring cells at time $t - 1$. To further test whether the statement is statistically significant, we compute the maximum likelihood estimator of the weights when the random fluctuation follows a Laplace distribution and generalized Gaussian distribution, with a different set of parameters at x and y coordinates.

As shown in Fig. 5(h), the maximum likelihood estimators of weights $w_x(t)$ and $w_y(t)$ are both smaller than 1. Furthermore, the shaded area shows that the 95% confidence intervals of the estimation, which is calculated by the residual bootstrap estimate [58]. In all plots, we found the upper bounds of the 95% confidence intervals of $w_x(t)$ and $w_y(t)$ are smaller than 1 at any time frame, indicating that the velocity of a cell aligns with the velocity of neighboring cells, while the velocity alignment is offset by other forces, such as frictional force between substrates and cells, which has also been noted in other studies [13, 23, 59, 60].

F. Summary of data-driven findings and model development

Here, we summarize the discovery from the EDA and statistical tests. First, variances of the random motion along the x and y coordinates are distinct, and both decrease over time due to cell proliferation. Second, the probability density of the velocity distribution at either the x coordinate or y coordinate has shown non-Gaussian behavior with a heavy tail and spiky mode near zero. Third, excluding cells with the opposite velocity substantially improves the correlation between cellular velocity and mean velocity of the neighboring cells at the previous time step, as cells glide across each other in a manner reminiscent of intercalation [61]. Fourth, the slope of the coefficient of a linear fit between the particle density and mean of neighboring particles in the prior time frame is smaller than one, indicating velocity alignment with its neighboring particles is offset by cell-substrate forces. All of the statistical tests we have developed so far are not restricted to the context of externally guided alignment; they are generally applicable to video microscopy which contains rich spatiotemporal data. Next, we illustrate how these analyses can be utilized to develop simulation models and parameter estimation for these models.

III. MODEL CONSTRUCTED FROM SELECTED FEATURES AND MAXIMUM LIKELIHOOD ESTIMATION

Our objective is to develop a minimum physical model that can account for temporally dependent orientational order parameters and velocities. We begin our model construction based on the seminal work by Vicsek [21], consisting of agents moving at a constant speed and updating their direction of movement at each step. The “new” direction is determined by the summation of the average of the velocities of neighboring agents, plus a random fluctuation. Despite its simplicity, this system exhibits a wide range of phenomena, including a transition from disordered to ordered behavior by adjusting the magnitude of the fluctuation. Later modification to this model includes introducing distance-dependent interac-

tions [23], which reproduces phenomena such as local cohesion [57] and jamming transitions [62], characteristic of a migrating epithelium [63], which has strong cell-cell junctions. Our statistical analysis provides insights into the discrepancy between the classical Vicsek model and the experimental results presented in this study.

We have utilized a data-driven approach to make systematic improvements to the Vicsek model by incorporating the four selected features into the model. Though each of these aspects has been noted to some extent in literature, to our knowledge, there has been no work incorporating all of them and systematically testing their applicability for reproducing the evolving orientational order observed in the experiment quantitatively. As part of our analysis, we will compare our model with those that do not encompass all of these aspects.

The velocity vector of the i th particle at time frame t , $\mathbf{v}_i(t) = (v_{i,x}(t), v_{i,y}(t))^T$, for $t = 1, \dots, T$ and $i = 1, \dots, n_t$, is modeled as

$$v_{i,x}(t) = w_x(t)\bar{v}_{i,x}(t-1) + \epsilon_{i,x}(t), \quad (2)$$

$$v_{i,y}(t) = w_y(t)\bar{v}_{i,y}(t-1) + \epsilon_{i,y}(t), \quad (3)$$

where $\epsilon_{i,x}(t)$ and $\epsilon_{i,y}(t)$ are independent zero-mean random variables with variances $\mathbb{V}[\epsilon_{i,x}(t)] = \tau_x^2(t)$ and $\mathbb{V}[\epsilon_{i,y}(t)] = \tau_y^2(t)$, respectively, $\bar{v}_{i,x}(t-1)$ and $\bar{v}_{i,y}(t-1)$ are the mean of the x and y directional velocities of neighboring particles at time $t-1$, $w_x(t)$ and $w_y(t)$ are real-valued scalars denoting the weights. The mean of the velocity at the x and y coordinates is modeled by

$$\bar{v}_{i,x}(t-1) = \frac{\sum_{j \in ne_i(t-1)} v_{j,x}(t-1)}{p_{ne_i(t-1)}}, \quad (4)$$

$$\bar{v}_{i,y}(t-1) = \frac{\sum_{j \in ne_i(t-1)} v_{j,y}(t-1)}{p_{ne_i(t-1)}}, \quad (5)$$

where $ne_i(t-1)$ is the neighboring set of cell i at time frame $t-1$ and $p_{ne_i(t-1)}$ is the number of cells in the neighboring set. We denote $\mathbf{s}_i(t-1)$ to be the 2D position of cell i at time frame $t-1$. The neighboring set is defined as $ne_i(t-1) = \{j : \|\mathbf{s}_j(t-1) - \mathbf{s}_i(t-1)\| < r \text{ and } \mathbf{v}_j(t-1) \cdot \mathbf{v}_i(t-1) > 0\}$, which contains the particles within a radius distance r but excludes particles with opposite velocities.

Section 2 IIC provides compelling evidence that the fluctuation distribution in the model significantly deviates from Gaussian distributions. Therefore, we introduce two distributions to model the random fluctuations in velocity: the Laplace distribution (or the double exponential distribution) and the generalized Gaussian distribution (or the stretched exponential distribution). Both distributions have been fit to the probability distribution of displacements that go beyond Gaussian assumptions, particularly when the system approaches jamming [38, 42, 64, 65]. Yet, finding the maximum likelihood estimator of the parameters with non-Gaussian fluctuations is not a computationally trivial task, given that the video contains 10^2 time frames and each frame has over 2000

cells. Hence, we introduce computationally-scalable approaches to compute the maximum likelihood estimator for models with these non-Gaussian fluctuations.

A. Maximum likelihood estimator with Laplace fluctuation

For the sake of simplicity, we will only demonstrate the model using velocity along the x direction as an example. The model for results along the y direction can be constructed in a similar manner. To model the fluctuation by the Laplace distribution $\epsilon_{i,x}(t) \sim \text{Laplace}(0, \tau_x(t))$, entails that the residual of velocity of particle i at time t $e_{i,x}(t) = v_{i,x}(t) - w_x(t)\bar{v}_{i,x}(t-1)$ follows

$$p(e_{i,x}(t) | \tau_x(t)) = \frac{1}{\sqrt{2}\tau_x(t)} \exp\left(-\frac{\sqrt{2}|e_{i,x}(t)|}{\tau_x(t)}\right). \quad (6)$$

The maximum likelihood estimator of $w_x(t)$ can be obtained by iterative algorithms such as the expectation-maximization algorithm and iterative reweighted least squared algorithm [66, 67], while a faster alternative is through linear programming [68, 69]. The likelihood function and the maximum likelihood estimator of the weight parameter, $\hat{w}_x(t)$, are introduced in Appendix A. The maximum likelihood estimator of the standard deviation of the random fluctuation can be obtained by maximizing the profile likelihood after substituting in $\hat{w}_x(t)$:

$$\hat{\tau}_x(t) = \frac{\sqrt{2}}{n_t} \sum_{i=1}^{n_t} |v_{i,x}(t) - \hat{w}_x(t)\bar{v}_{i,x}(t-1)|. \quad (7)$$

B. Maximum likelihood estimator with generalized Gaussian distribution

In general, both the Laplace and the Gaussian distribution are special cases of the generalized Gaussian distribution (GGD), also referred to as a stretched exponential distribution [70, 71]. Here, we illustrate the formulation by applying the model to fit the velocity component along the x direction. We assume that the residual $e_{i,x}(t)$ follows a zero-mean GGD with parameter $\alpha_x(t)$ and $\beta_x(t)$ at time frame t :

$$p(e_{i,x}(t) | \alpha_x(t), \beta_x(t)) = \left(\frac{\beta_x(t)}{2\alpha_x(t)\Gamma\left(\frac{1}{\beta_x(t)}\right)}\right) \exp\left\{-\left(\frac{|e_{i,x}(t)|}{\alpha_x(t)}\right)^{\beta_x(t)}\right\}. \quad (8)$$

The variance of the GGD follows $\tau_x^2(t) = \mathbb{V}[e_{i,x}(t)] = \alpha_x^2(t)\Gamma(3/\beta_x(t))/\Gamma(1/\beta_x(t))$, with $\Gamma(\cdot)$ denoting the Gamma function. When $\beta_x(t) = 2$ and $\alpha_x(t) = \sqrt{2}\tau_x(t)$, GGD reduces to a Gaussian distribution. When $\beta_x(t) = 1$ and $\alpha_x(t) = \tau_x(t)/\sqrt{2}$, GGD reduces to a Laplace distribution. Therefore, the shape parameter $\beta_x(t)$ controls

how close the GGD resembles a Gaussian distribution. Similarly, the GGD of the residual along y can also be defined in terms of parameter $\alpha_y(t)$ and $\beta_y(t)$ at any given time frame t .

It should be noted that at each time frame, the GGD has three parameters, and some of these parameters, such as the power parameters, are notoriously difficult to estimate accurately [72]. Hence, we derive closed-form derivatives to numerically compute the maximum likelihood estimator of the parameters, introduced in Appendix B.

IV. RESULTS

A. Details on simulation

We first briefly introduce the setup of the simulation: Cells are modeled as particles, and their initial velocities and positions are imported from the data. For simplicity, we assume that the cell number remains constant. We start by partitioning the space into grids, and the spacing between gridlines is no smaller than the cell-cell interaction radius r . In our simulation, grids are populated with cells based on cells' positions $\mathbf{s}_i(t) = (s_{i,x}(t), s_{i,y}(t))^T$ (Fig. 1(e)). The grid-based approach improves computational efficiency since as such, identifying a cell's neighbors only requires searching the nine grids surrounding it. Using this method, computing the likelihood function for parameter estimation and simulation only requires $\mathcal{O}(\sum_{t=1}^T n_t)$ operations, which is much faster than the conventional approach requiring $\mathcal{O}(\sum_{t=1}^T n_t^2)$ operations, where n_t is the number of cells at time frame t .

The velocities $v_{i,x}(t)$ and $v_{i,y}(t)$ are updated according to Eqs. (2)-(3), with 3 types of distribution of fluctuations: Gaussian, Laplace, or GGD, 2 types of neighbors: interactions with all neighboring cells or only neighboring cells with the same direction velocity, and weights (ω_x and ω_y) of the interaction fixed to be 1 or estimated from the data. All parameters are estimated based on the maximum likelihood estimators introduced in Section III.

B. Model comparison by simulated orientational order parameter and velocity variability

We compare models using simulated order parameters and variability of velocity. The simulated order parameters is computed by $S(t) = \langle \cos(2\tilde{\theta}_i(t)) \rangle_i$ with $\tilde{\theta}_i(t)$ defined in Eq. (1). As velocity distribution more closely resembles a Laplace distribution, we use the average absolute deviation or L_1 loss to measure the variability of velocity: $\tilde{\sigma}_x(t) = \frac{1}{n_t} \sum_{i=1}^{n_t} |v_{i,x}(t) - \bar{v}_x(t)|$ and $\tilde{\sigma}_y(t) = \frac{1}{n_t} \sum_{i=1}^{n_t} |v_{i,y}(t) - \bar{v}_y(t)|$ with $\bar{v}_x(t) \approx 0$ and $\bar{v}_y(t) \approx 0$, instead of the more commonly used variance or L_2 loss to quantify the variability of the velocity. This is because the velocity distribution is closer to a Laplace

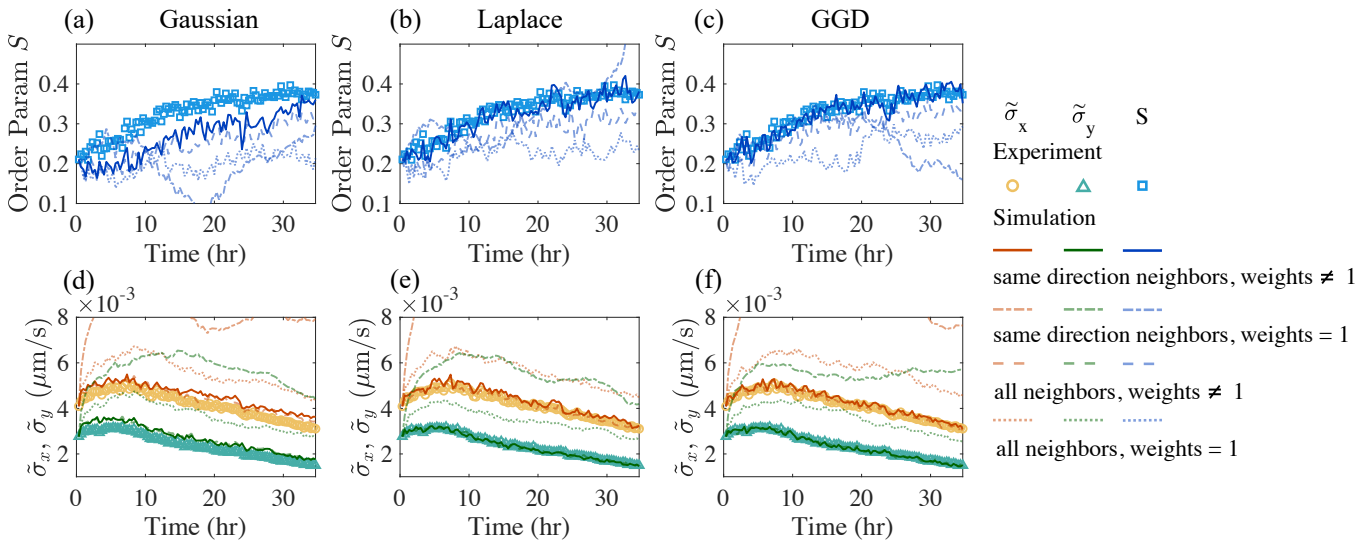


FIG. 6. Reproducing orientational order parameters and mean absolute deviation of velocity with different simulation models at a representative radius $r = 75 \mu\text{m}$. The left, middle, right panels compare simulations using the Gaussian, Laplace, GGD fluctuation with experimental observations. For each type of fluctuation distributions, simulations of different interaction rules are presented. (a-c) show the orientational order parameter, (d-f) show the average absolute deviation of the velocities.

distribution than a Gaussian distribution (Fig. 2(b) and (c)), and thus the L_1 loss is more appropriate to account for the variability of the distribution.

In Fig. 6, we present the results of the particle-based simulation, from which we computed the dynamics of the orientational order parameters and the average absolute deviation of the velocity. We then compared these results to the experiments. We apply the estimation and simulation procedure to scenarios where either all features are present or one or more of them are missing. Remarkably, we find simple models from Eqs. (2)-(3) with four features found in Section II A can reproduce the dynamical progression of order parameters (solid curves in Fig. 6(b) and (c)) and average absolute deviation of the velocity (Fig. 6(e) and (f)), even though we do not fit a loss function for these ensemble properties directly. In Fig. 12 and Fig. 13 in Appendix C, we show the simulation using the estimated parameters from two other experiments and observe that our model is sufficiently general to capture the progression of system characteristics with varying initial densities and substrate materials.

In all simulation models, the magnitude and variability of the velocity along the x coordinate are both larger than those along the y coordinate, stemming from our first finding that the velocity distribution is anisotropic. The growing anisotropy of the velocity induced by the molecularly aligned substrate leads to the increase of orientational order parameters.

Second, the simulation with neighbor ensembles that include cells with the same direction (solid curves in Fig. 6) more accurately reproduces both the progression of the orientational order and velocity than the simulation with interactions that includes all particles within a ra-

dius distance. This confirms the finding from Fig. 5(g), which shows that the model with neighbor that includes cells with the same direction can better predict the cellular velocity in the next time frame. This effect likely occurs because of the complex interplay of cell-cell interactions, which are mediated through a cascade of signaling molecules. As a result, the direction and polarity of contact are crucial factors in determining the strength of cell-cell interaction [55].

Third, the weight parameters $w_x(t)$ and $w_y(t)$ estimated by observations are always smaller than 1 (Fig. 5(h)). In the simulation, we find that the model with estimated weights typically outperforms the model where the weights are constrained to be 1, particularly for reproducing the dynamical progression of the average absolute deviation of the velocity (Fig. 6(a-c)). If the estimated slope parameters are equal to 1, the simulated velocity magnitude is frequently larger than what is observed. In comparison, the inclusion of the estimated weights appears to resolve this issue, as the velocity is constrained. Furthermore, a unique aspect of our formulation is that the variability of velocity can change over time, which enables us to capture a wider array of behaviors, such as slow-downs. For instance, with increasing cell density, the average magnitude of the velocity must change. Ultimately, crowding leads to arrested dynamics [5]. Nonetheless, simulation models often oversimplify this aspect by only modeling the velocity angle, overlooking the important role of slow-downs or heterogeneous dynamics [21, 25].

Lastly, we find that the simulation model validates the finding that velocities are not normally distributed (Fig. 4)—the model with fluctuations following Laplace distri-

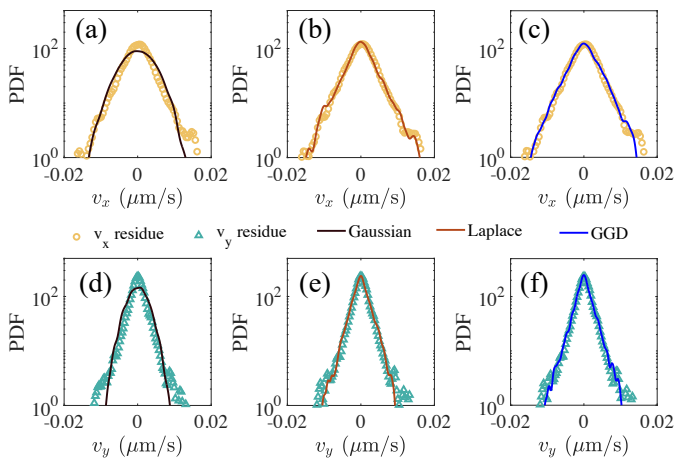


FIG. 7. Distributions of random fluctuations between the observations and simulated models at a representative radius $r = 75 \mu\text{m}$ and time $t = 20$ hours with the distributions of the fluctuation in the simulation following Gaussian (a,d), Laplace (b,e) and GGD (c,f).

butions (Fig. 6(b)) better reproduces the progression of the orientational order parameter than the model with Gaussian fluctuation (Fig. 6(a)), even if they contain the same number of fitting parameters. On the other hand, the model with GGD fluctuation (Fig. 6(c)) fits slightly better than the one with Laplace fluctuation, but it also contains an additional parameter at each time point than the other two distributions, and thus it has more flexibility in controlling the decay of the tail of the distribution. It is important to note that reproducing solely the variability of the velocity is inadequate to replicate the velocity orientational order parameter in our system, which is sensitive to the change in the velocity distribution. Here we use a neighbor radius of $r = 75 \mu\text{m}$. We show that radius also plays a role in refining the fit, but to a much lesser degree (Table I).

To further explore the difference between the effect of different random fluctuation distributions, in Fig. 7, we show the distribution of the simulated residuals in x direction in (a-c): $e_{i,x}^{sim} = v_{i,x}^{sim}(t) - \hat{w}_x(t)\bar{v}_{i,x}^{sim}(t-1)$ and in y direction in (d-f): $e_{i,y}^{sim} = v_{i,y}^{sim}(t) - \hat{w}_y(t)\bar{v}_{i,y}^{sim}(t-1)$ by the colored circles and triangles, and the solid curve denotes the distribution of the residuals in the simulations. The fitted weight is derived from the maximum likelihood estimator where the fluctuations follow Gaussian, Laplace, and GGD, from the left to the right. Simulated Gaussian fluctuation distributions along x and y directions are shown in Fig. 7(a) and (d), which underestimates the number of cells with near-zero velocities in both directions. Instead, simulation fluctuation distributions with either Laplace distribution or GGD better reproduce the experiments, as shown in Fig. 6(b), (c), (e) and (f).

We present a summary of the results of incorporating various modeling parameters and compare the sim-

TABLE I. RMSE_S for the orientational order parameter estimates. All assumed the weights parameters from the fluctuation from the x and y directions are separately estimated. The standard deviation of the velocity orientational order parameter is 0.050 and an effective method (highlighted in bold typeface) has RMSE smaller than this value. AN (= all neighbors) and SDN (= same direction neighbor) stand for methods with all neighboring cells within the radius and the same direction neighboring cells, respectively. Gau, Lap, and GGD are Gaussian, Laplace, and generalized Gaussian distributions of the fluctuation.

Orientational order parameter	$\omega = 1$			$\omega \neq 1$		
	Gau	Lap	GGD	Gau	Lap	GGD
$r = 25 \mu\text{m}$ AN	0.17	0.12	0.14	0.090	0.061	0.058
$r = 25 \mu\text{m}$ SDN	0.12	0.16	0.14	0.077	0.034	0.038
$r = 50 \mu\text{m}$ AN	0.11	0.13	0.12	0.079	0.047	0.043
$r = 50 \mu\text{m}$ SDN	0.041	0.12	0.033	0.069	0.022	0.025
$r = 75 \mu\text{m}$ AN	0.13	0.11	0.10	0.081	0.058	0.042
$r = 75 \mu\text{m}$ SDN	0.15	0.060	0.099	0.063	0.020	0.018

ulation to the experimentally obtained orientational order parameter in Table I. The root mean squared error (RMSE) of the velocity orientational order parameter is calculated as the following:

$$\text{RMSE}_S = \sqrt{\sum_{t=1}^T \frac{(S_t^* - S_t)^2}{T}}, \quad (9)$$

where S_t^* and S_t are the ensemble orientational order parameters from the simulation and experiments at time frame t , respectively. The RMSE for $\tilde{\sigma}_x$ and $\tilde{\sigma}_y$ can be defined similarly, and they are shown in Table II. RMSE values that are better than the baseline average absolute deviation are bolded. Values from Table I and II indicate that, while there are several effective methods to describe the average absolute deviation of velocity, it is more difficult to capture the progression of the order parameter. This is not surprising as the order parameter is a complex function of the distribution, which is not explicitly controlled by any parameters in the likelihood function, given $v_{i,x}$ and $v_{i,y}$ are modeled independently. When modeling the velocity fluctuation, approaches incorporating Laplace and GGD fluctuations better capture the progression of the orientational order parameter, which is the main characteristic of the system, compared to the model with the Gaussian fluctuation.

C. Sensitivity analysis of the simulation

As captured by Eqs. (2) and (3), the anisotropy of substrate materials induces asymmetric velocities in cells, which are manifested through both interactions and fluctuations. These contributions are temporally dependent, as changes in cell density due to proliferation lead to

TABLE II. RMSE for the average absolute deviation of the velocity estimates $\tilde{\sigma}_x$ and $\tilde{\sigma}_y$. All assumed the weights parameters from the fluctuation from the x and y directions are separately estimated. The benchmark RMSE of the average absolute deviation (calculated by the standard deviation of the average absolute deviation) for $\tilde{\sigma}_x$, $\tilde{\sigma}_y$ are 5.7×10^{-4} and 5.3×10^{-4} , respectively. An effective method (highlighted in bold typeface) has RMSE smaller than this value. AN (= all neighbors) and SDN (= same direction neighbor) stand for methods with all neighboring cells within the radius and the same direction neighboring cells, respectively. RMSE = (table value) $\times 10^{-4}$.

Average absolute deviation of velocity estimates RMSE $_{\tilde{\sigma}_x}$, RMSE $_{\tilde{\sigma}_y} \times 10^4$	$\omega = 1$						$\omega \neq 1$					
	Gaussian		Laplace		GGD		Gaussian		Laplace		GGD	
	$\tilde{\sigma}_x$	$\tilde{\sigma}_y$										
$r = 25 \mu\text{m AN}$	38	35	38	30	39	32	1.1	2.7	1.4	0.56	1.3	0.67
$r = 25 \mu\text{m SDN}$	137	68	140	59	130	63	3.0	3.5	2.9	1.1	2.6	1.4
$r = 50 \mu\text{m AN}$	24	20	20	17	25	20	2.4	3.1	0.83	0.52	0.89	0.54
$r = 50 \mu\text{m SDN}$	74	40	88	36	77	37	3.4	3.4	2.4	0.67	1.7	0.83
$r = 75 \mu\text{m AN}$	14	14	14	12	16	13	3.0	3.6	0.87	0.47	0.72	0.53
$r = 75 \mu\text{m SDN}$	42	34	52	32	49	32	3.9	3.4	2.1	0.56	1.5	0.51

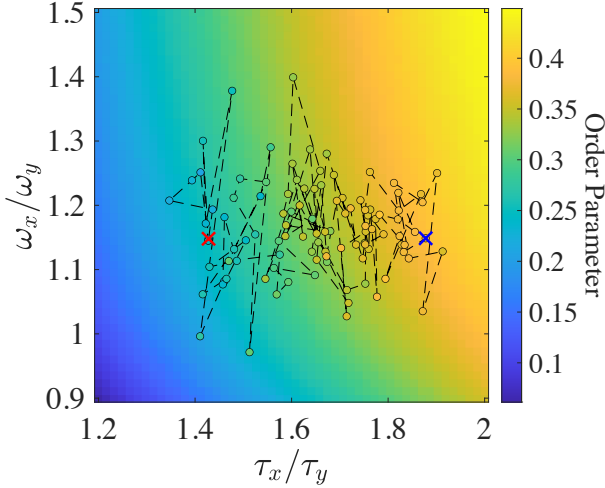


FIG. 8. Change of order parameters due to the change of simulation parameters with $\tau_x = 0.02$ and $w_x = 0.7$. The color bar corresponds to the simulated order parameter at long times. The dashed lines and circles denote the actual path of the experimental results plotted against the phase diagram. The colors of the markers correspond to the order parameter as denoted by the color bar. Red and blue X's denote the beginning and the end of the trajectory.

fluctuations in the velocity magnitude. For a given set of model parameters and fluctuation distribution, it will be helpful to understand their impacts on the asymptotic order parameters, such as those that can be achieved after enough time has elapsed, for refining experimental designs and controls.

Here, we perform a sensitivity analysis for simulation with Laplace fluctuations and all other selected features. We vary the ratio of the variance of the fluctuation τ_x/τ_y and the ratio of their weights ω_x/ω_y in the model (Eqs. (2) and (3)). While the variation of the order parameter is controlled by four parameters (τ_x , τ_y , ω_x , and

ω_y), we find that the estimated ω_x (Fig. 5(h)) does not change drastically over time. Furthermore, we show in Figs. 10(a) and (b) that simulations with two different choices of τ_x do not have a large impact on the variation of the order parameter so long as the ratios of ω 's and τ 's remain the same. Hence, we are able to represent the asymptotic value of the order parameter on a 2D plot with $\tau_x = 0.02$ and $\omega_x = 0.7$ fixed to be the mean of estimation over all time frames. Each simulation is implemented in 70 time points, where the order parameter fully equilibrates after 20 time points (see the evolution of the order parameter for select simulation parameter in Fig. 11). Due to this, the order value in the reported colormap was computed by averaging the last 50 time points.

We find that the asymptotic order parameter increases when either τ_x/τ_y or ω_x/ω_y increases (Fig. 8). The order parameters computed from the experiment at different time points are overlaid on top of the diagram, where the warmer colors represent a larger magnitude of the order parameter, consistent with the color scheme of the phase diagram. The ratio of ω_x/ω_y fluctuates around a fixed value ~ 1.2 , potentially due to fixed properties of the external substrate guiding cells to migrate preferentially along x . That is to say, the substrate has a fixed modulus ratio along the x and y directions, as found in [20]. This ratio is reflected in the variance of the velocity along the corresponding directions, thereby restricting their ratio. As the system evolves over time, the caging effect becomes more prominent along y , which increases the ratio of τ_x/τ_y . This analysis provides further evidence to support our conclusion that substrate anisotropy and cell crowding both influence alignment. However, at low cell densities, the alignment effect is likely drowned out by noise. Our findings also open up exciting design opportunities, where τ_x/τ_y can potentially be controlled by varying the initial cell density or the composition of the substrate [19], so the cell alignment dynamics can be tuned as a result. Overall, good agreements between the

experiment and simulation are obtained.

V. DISCUSSIONS

Cells can be induced to form aligned structures through a complex cascade of physiochemical signaling processes in both *in vitro* and *in vivo* settings. Experiments have shown that cells can migrate preferentially following the molecular orientation of the substrate. This preferential migration results from two interrelated effects: cell polarization due to the substrate and crowding due to the presence of other cells. Cell polarization occurs due to anisotropic interactions between the cell and the substrate or the extracellular matrix, including friction, damping, binding, and directional proliferation. Crowding further promotes alignment. Aligned structures have been shown to increase the speed and persistence of cell migration, while migration speed is also influenced by cell shape and the surrounding topography [73, 74].

Here we extract cell-level behaviors from massive single-cell migration data that allow for characterization, estimation, and ultimately prediction of active dynamics. Rather than relying on predetermined forms of cell-cell interaction and simulating displacement data, as is often done in conventional modeling methods, we propose a hybrid approach that combines data-driven methods to select features and expand a baseline physics model, namely the Vicsek model, by utilizing these selected features. Our findings highlight the importance of anisotropic, non-Gaussian distributions of velocities in reproducing the progression of cell movements guided by the molecularly aligned substrates. Of equal importance is the construction of neighboring interaction, by eliminating contributions from cells with opposite velocities and applying weights different from unity. These features are reminiscent of recent works that take into account the directionality of cell-cell instantaneous velocity in modeling interaction, particularly in the context of cell-extracellular matrix interaction [75], and models that include contact-induced inhibition [13, 76, 77].

The shape of the probability density of the temporally dependent velocity has a significant impact on accurately reproducing orientational order parameters and velocities through simulation. In standard diffusions, the probability density of displacement at any lag time is typically represented by a Gaussian distribution, as stated in references such as [43, 78, 79]. However, we observe that the experimental velocity distribution vastly deviates from a Gaussian distribution (Fig. 4). The velocity distributions comprise a considerable number of cells that have undergone minimal movement, along with a significant number of cells that have moved a substantially long distance over a specific time interval h . Non-Gaussian distribution of displacement has previously been reported in systems with heterogeneous dynamics, as noted in [37, 80]. The high concentration of immobile cells centered at zero can be attributed to particles that are con-

finned by their neighbors. On the other hand, the presence of heavy tails of the velocity distribution can be attributed to the coordinated movements of many particles, also known as “jumps”, as discussed in [42]. Empirical studies have also shown that a significant jump is often followed by other jumps [36]. Consequently, these probability densities exhibit slower rates of decay in the tail of the distribution compared to a Gaussian distribution, whereas they are more appropriately captured by a Laplace distribution [38] or a generalized Gaussian distribution. Although various experiments have shown anomalous distributions of displacement probability [36–38, 80], it has been less recognized that the distribution of random fluctuations plays a critical role in reproducing the progression of orientational order parameters observed in the experiments, partly because of a lack of means of efficient parameter estimation. Our work has filled in this gap by developing a maximum likelihood estimator for model parameters and a fast simulation scheme for non-Gaussian dynamics with the estimated parameters.

Our analysis has also revealed that the distinct behaviors of cells on isotropic or nematic substrates can be largely attributed to the presence or absence of anisotropic velocity. Our model captures this phenomenon by demonstrating that a difference in variability of the velocity along x and y directions leads to alignment (Figs. 6 and 12), while cells on isotropic substrates do not develop any order (Figs. 13). We further show that asymptotic alignment can be controlled by the ratio of the weights and variance parameters (Fig. 8), and the order tends to approach zero as the velocity becomes more isotropic.

Our procedure has several distinctive features that showcase data-driven discovery. Rather than including all potential covariates, we begin by selecting the features to be included through exploratory data analysis and statistical tests. Such an approach produces more interpretable models and improves the efficiency of estimation, since only features with significant effects will be included in the model and parameter estimation. Second, we define a data generative model, instead of minimizing a loss function as conventionally adopted in other machine learning approaches. The data generative model provides a probabilistic mechanism, where the uncertainty of the estimation can be rigorously estimated and propagated throughout the analysis. Compared to physics-driven approaches, our method enables the discovery of new neighboring structures and non-Gaussian fluctuations, which we later demonstrate to be the key ingredients to capture the progression of alignment dynamics. This new hybrid approach can be utilized in other systems to aid physicists in automating the tasks of visualization and feature selection, and extending baseline physics models by incorporating the selected features.

Our model bridges the gap between trajectory information and stochastic collective behaviors. A few additional directions are of interest for future work. These include

how to interpret the diminished influence of opposite-direction neighbors using the collision model, the mechanism behind non-Gaussian distribution velocities, and how cell proliferation contributes to observed trends in the variance. Future work could explore fruitful avenues by proceeding in the following directions.

Although the current model takes into account the influence of neighboring cells on velocity changes, it is important to note that cells also exhibit persistent motion as they travel, resulting in relatively smooth, one-dimensional spatial patterns [54, 81]. To fully capture the spatial patterns of these cells, it will be necessary to incorporate their self-persistent motion in future studies. On the other hand, the effect of increasing cell count and the corresponding slow-down as the system approaches jamming must be more carefully modeled in order to effectively forecast the variance of the velocity fluctuation.

Ultimately, the velocity changes are governed by forces [82–84]. Direct, in-situ force measurements will help further elucidate mechanisms and refine our models. Efforts must be made to reconcile the anisotropic nature of the substrate that induces cell alignment with the isotropic assumption often made in mechanical analysis to deduce force, as in the case of traction force microscopy

[85]. Other important considerations that should also be integrated or at least studied in conjunction are cell shapes and the restructuring of their sub-cellular structures. When tracking cell migration, we largely rely on fitting an ellipse to the nuclei. In order to monitor the dynamics of aforementioned features, algorithms without particle tracking, such as Fourier-based differential dynamic microscopy [86], can be applied to extracting system properties such as mean squared displacements, for inspecting the mechanical properties of the systems.

VI. ACKNOWLEDGEMENTS

The experimental portion of this work was supported by the Otis Williams Postdoctoral Fellowship from the Division of Mathematical, Life, & Physical Sciences in the College of Letter & Science, with partial support from the BioPACIFIC Materials Innovation Platform of the National Science Foundation under the Award No. DMR-1933487 (NSF BioPACIFIC MIP). MG acknowledges partial support from the National Science Foundation under Award No. 2053423. The authors thank Cristina Marchetti, Megan Valentine, and Matt Helgeson for helpful discussions.

-
- [1] M. C. Marchetti, J.-F. Joanny, S. Ramaswamy, T. B. Liverpool, J. Prost, M. Rao, and R. A. Simha, *Hydrodynamics of soft active matter*, *Reviews of modern physics* **85**, 1143 (2013).
- [2] T. Sanchez, D. T. Chen, S. J. DeCamp, M. Heymann, and Z. Dogic, *Spontaneous motion in hierarchically assembled active matter*, *Nature* **491**, 431 (2012).
- [3] S. Ramaswamy, *Active matter*, *Journal of Statistical Mechanics: Theory and Experiment* **2017**, 054002 (2017).
- [4] H. Yang, A. F. Pegoraro, Y. Han, W. Tang, R. Abeyaratne, D. Bi, and M. Guo, *Configurational fingerprints of multicellular living systems*, *Proceedings of the National Academy of Sciences* **118**, e2109168118 (2021).
- [5] T. E. Angelini, E. Hannezo, X. Trepate, M. Marquez, J. J. Fredberg, and D. A. Weitz, *Glass-like dynamics of collective cell migration*, *Proceedings of the National Academy of Sciences* **108**, 4714 (2011).
- [6] P.-F. Lenne and V. Trivedi, *Sculpting tissues by phase transitions*, *Nature Communications* **13**, 1 (2022).
- [7] A. Ray, R. K. Morford, N. Ghaderi, D. J. Odde, and P. P. Provenzano, *Dynamics of 3D carcinoma cell invasion into aligned collagen*, *Integrative biology* **10**, 100 (2018).
- [8] L. C. Biggs, C. S. Kim, Y. A. Miroshnikova, and S. A. Wickström, *Mechanical forces in the skin: roles in tissue architecture, stability, and function*, *Journal of Investigative Dermatology* **140**, 284 (2020).
- [9] M. W. Ferguson and S. O’Kane, *Scar-free healing: from embryonic mechanisms to adult therapeutic intervention*, *Philosophical Transactions of the Royal Society of London. Series B: Biological Sciences* **359**, 839 (2004).
- [10] S. Sarkar, G. Y. Lee, J. Y. Wong, and T. A. Desai, *Development and characterization of a porous micro-patterned scaffold for vascular tissue engineering applications*, *Biomaterials* **27**, 4775 (2006).
- [11] J. S. Choi, Y. Piao, and T. S. Seo, *Circumferential alignment of vascular smooth muscle cells in a circular microfluidic channel*, *Biomaterials* **35**, 63 (2014).
- [12] T. D. Hinnant, J. A. Merkle, and E. T. Ables, *Coordinating proliferation, polarity, and cell fate in the drosophila female germline*, *Frontiers in cell and developmental biology* **8**, 19 (2020).
- [13] B. A. Camley, J. Zimmermann, H. Levine, and W.-J. Rappel, *Emergent collective chemotaxis without single-cell gradient sensing*, *Physical Review Letters* **116**, 098101 (2016).
- [14] A. J. Ridley, M. A. Schwartz, K. Burridge, R. A. Firtel, M. H. Ginsberg, G. Borisy, J. T. Parsons, and A. R. Horwitz, *Cell migration: integrating signals from front to back*, *Science* **302**, 1704 (2003).
- [15] R. Tonndorf, D. Aibibu, and C. Cherif, *Isotropic and anisotropic scaffolds for tissue engineering: Collagen, conventional, and textile fabrication technologies and properties*, *International Journal of Molecular Sciences* **22**, 9561 (2021).
- [16] G. Grégoire, H. Chaté, and Y. Tu, *Moving and staying together without a leader*, *Physica D: Nonlinear Phenomena* **181**, 157 (2003).
- [17] T. Turiv, J. Krieger, G. Babakhanova, H. Yu, S. V. Shiyankovskii, Q.-H. Wei, M.-H. Kim, and O. D. Lavrentovich, *Topology control of human fibroblast cells monolayer by liquid crystal elastomer*, *Science Advances* **6**, eaaz6485 (2020).
- [18] G. Babakhanova, J. Krieger, B.-X. Li, T. Turiv, M.-H. Kim, and O. D. Lavrentovich, *Cell alignment by smectic*

- liquid crystal elastomer coatings with nanogrooves, *Journal of Biomedical Materials Research Part A* **108**, 1223 (2020).
- [19] D. Martella, L. Pattelli, C. Matassini, F. Ridi, M. Bonini, P. Paoli, P. Baglioni, D. S. Wiersma, and C. Parmegiani, Liquid crystal-induced myoblast alignment, *Advanced healthcare materials* **8**, 1801489 (2019).
- [20] Y. Luo, M. Gu, M. Park, X. Fang, Y. Kwon, J. M. Uruña, J. R. de Alaniz, M. E. Helgeson, M. C. Marchetti, and M. T. Valentine, Molecular-scale substrate anisotropy and crowding drive long-range nematic order of cell monolayers, arXiv preprint arXiv:2210.13425 (2022).
- [21] T. Vicsek, A. Czirók, E. Ben-Jacob, I. Cohen, and O. Shochet, Novel type of phase transition in a system of self-driven particles, *Physical Review Letters* **75**, 1226 (1995).
- [22] J. Toner and Y. Tu, Flocks, herds, and schools: A quantitative theory of flocking, *Physical review E* **58**, 4828 (1998).
- [23] B. Szabo, G. Szöllösi, B. Gönci, Z. Jurányi, D. Selmeczi, and T. Vicsek, Phase transition in the collective migration of tissue cells: experiment and model, *Physical Review E* **74**, 061908 (2006).
- [24] H. Chaté, F. Ginelli, G. Grégoire, and F. Raynaud, Collective motion of self-propelled particles interacting without cohesion, *Physical Review E* **77**, 046113 (2008).
- [25] F. Ginelli, F. Peruani, M. Bär, and H. Chaté, Large-scale collective properties of self-propelled rods, *Physical Review Letters* **104**, 184502 (2010).
- [26] X. Li, R. Balagam, T.-F. He, P. P. Lee, O. A. Igoshin, and H. Levine, On the mechanism of long-range orientational order of fibroblasts, *Proceedings of the National Academy of Sciences* **114**, 8974 (2017).
- [27] J. Bongard and H. Lipson, Automated reverse engineering of nonlinear dynamical systems, *Proceedings of the National Academy of Sciences* **104**, 9943 (2007).
- [28] D. B. Brückner, N. Arlt, A. Fink, P. Ronceray, J. O. Rädler, and C. P. Broedersz, Learning the dynamics of cell-cell interactions in confined cell migration, *Proceedings of the National Academy of Sciences* **118**, e2016602118 (2021).
- [29] I.-C. Chou and E. O. Voit, Recent developments in parameter estimation and structure identification of biochemical and genomic systems, *Mathematical biosciences* **219**, 57 (2009).
- [30] S. H. Rudy, S. L. Brunton, J. L. Proctor, and J. N. Kutz, Data-driven discovery of partial differential equations, *Science advances* **3**, e1602614 (2017).
- [31] P. A. Reinbold, D. R. Gurevich, and R. O. Grigoriev, Using noisy or incomplete data to discover models of spatiotemporal dynamics, *Physical Review E* **101**, 010203 (2020).
- [32] J. Colen, M. Han, R. Zhang, S. A. Redford, L. M. Lemma, L. Morgan, P. V. Ruijgrok, R. Adkins, Z. Bryant, Z. Dogic, *et al.*, Machine learning active-nematic hydrodynamics, *Proceedings of the National Academy of Sciences* **118**, e2016708118 (2021).
- [33] M. Gu, X. Liu, X. Fang, and S. Tang, Scalable marginalization of correlated latent variables with applications to learning particle interaction kernels, *The New England Journal of Statistics in Data Science*, In Press (2022).
- [34] Y. Fily and M. C. Marchetti, Athermal phase separation of self-propelled particles with no alignment, *Physical Review Letters* **108**, 235702 (2012).
- [35] C. Bechinger, R. Di Leonardo, H. Löwen, C. Reichhardt, G. Volpe, and G. Volpe, Active particles in complex and crowded environments, *Reviews of Modern Physics* **88**, 045006 (2016).
- [36] B. Wang, S. M. Anthony, S. C. Bae, and S. Granick, Anomalous yet Brownian, *Proceedings of the National Academy of Sciences* **106**, 15160 (2009).
- [37] K. C. Leptos, J. S. Guasto, J. P. Gollub, A. I. Pesci, and R. E. Goldstein, Dynamics of enhanced tracer diffusion in suspensions of swimming eukaryotic microorganisms, *Physical Review Letters* **103**, 198103 (2009).
- [38] B. Wang, J. Kuo, S. C. Bae, and S. Granick, When Brownian diffusion is not Gaussian, *Nature materials* **11**, 481 (2012).
- [39] W. He, H. Song, Y. Su, L. Geng, B. J. Ackerson, H. Peng, and P. Tong, Dynamic heterogeneity and non-Gaussian statistics for acetylcholine receptors on live cell membrane, *Nature communications* **7**, 11701 (2016).
- [40] F. Ginelli, The physics of the vicsek model, *The European Physical Journal Special Topics* **225**, 2099 (2016).
- [41] J. Toner and Y. Tu, Long-range order in a two-dimensional dynamical XY model: how birds fly together, *Physical Review Letters* **75**, 4326 (1995).
- [42] P. Chaudhuri, L. Berthier, and W. Kob, Universal nature of particle displacements close to glass and jamming transitions, *Physical Review Letters* **99**, 060604 (2007).
- [43] W. Coffey and Y. P. Kalmykov, *The Langevin equation: with applications to stochastic problems in physics, chemistry and electrical engineering*, Vol. 27 (World Scientific, 2012).
- [44] G. Duclos, S. Garcia, H. Yevick, and P. Silberzan, Perfect nematic order in confined monolayers of spindle-shaped cells, *Soft matter* **10**, 2346 (2014).
- [45] R. Cerbino and V. Trappe, Differential dynamic microscopy: probing wave vector dependent dynamics with a microscope, *Physical Review Letters* **100**, 188102 (2008).
- [46] M. Gu, Y. Luo, Y. He, M. E. Helgeson, and M. T. Valentine, Uncertainty quantification and estimation in differential dynamic microscopy, *Physical Review E* **104**, 034610 (2021).
- [47] C. A. Schneider, W. S. Rasband, and K. W. Eliceiri, Nih image to imagej: 25 years of image analysis, *Nature methods* **9**, 671 (2012).
- [48] J. Löber, F. Ziebert, and I. S. Aranson, Collisions of deformable cells lead to collective migration, *Scientific reports* **5**, 1 (2015).
- [49] J. W. Tukey, *Exploratory data analysis*, Vol. 2 (Addison-Wesley, 1977).
- [50] G. E. Box, Non-normality and tests on variances, *Biometrika* **40**, 318 (1953).
- [51] S. S. Shapiro and M. B. Wilk, An analysis of variance test for normality (complete samples), *Biometrika* **52**, 591 (1965).
- [52] C. Guillot and T. Lecuit, Mechanics of epithelial tissue homeostasis and morphogenesis, *Science* **340**, 1185 (2013).
- [53] D. Bi, J. H. Lopez, J. M. Schwarz, and M. L. Manning, Energy barriers and cell migration in densely packed tissues, *Soft matter* **10**, 1885 (2014).
- [54] W.-J. Rappel and L. Edelstein-Keshet, Mechanisms of cell polarization, *Current opinion in systems biology* **3**, 43 (2017).

- [55] D. Li and Y.-l. Wang, Coordination of cell migration mediated by site-dependent cell–cell contact, *Proceedings of the National Academy of Sciences* **115**, 10678 (2018).
- [56] R. Mueller, J. M. Yeomans, and A. Doostmohammadi, Emergence of active nematic behavior in monolayers of isotropic cells, *Physical Review Letters* **122**, 048004 (2019).
- [57] H. Chaté, F. Ginelli, G. Grégoire, F. Peruani, and F. Raynaud, Modeling collective motion: variations on the vicsek model, *The European Physical Journal B* **64**, 451 (2008).
- [58] A. C. Davison and D. V. Hinkley, *Bootstrap methods and their application*, 1 (Cambridge university press, 1997).
- [59] N. Sepúlveda, L. Petitjean, O. Cochet, E. Grasland-Mongrain, P. Silberzan, and V. Hakim, Collective cell motion in an epithelial sheet can be quantitatively described by a stochastic interacting particle model, *PLoS computational biology* **9**, e1002944 (2013).
- [60] K. H. Nagai, Y. Sumino, R. Montagne, I. S. Aranson, and H. Chaté, Collective motion of self-propelled particles with memory, *Physical Review Letters* **114**, 168001 (2015).
- [61] R. J. Huebner and J. B. Wallingford, Coming to consensus: a unifying model emerges for convergent extension, *Developmental cell* **46**, 389 (2018).
- [62] S. Henkes, Y. Fily, and M. C. Marchetti, Active jamming: Self-propelled soft particles at high density, *Physical Review E* **84**, 040301 (2011).
- [63] E. Méhes and T. Vicsek, Collective motion of cells: from experiments to models, *Integrative biology* **6**, 831 (2014).
- [64] E. R. Weeks, J. C. Crocker, A. C. Levitt, A. Schofield, and D. A. Weitz, Three-dimensional direct imaging of structural relaxation near the colloidal glass transition, *Science* **287**, 627 (2000).
- [65] H. E. Castillo and A. Parsaeian, Local fluctuations in the ageing of a simple structural glass, *Nature physics* **3**, 26 (2007).
- [66] E. Schlossmacher, An iterative technique for absolute deviations curve fitting, *Journal of the American Statistical Association* **68**, 857 (1973).
- [67] R. F. Phillips, Least absolute deviations estimation via the EM algorithm, *Statistics and Computing* **12**, 281 (2002).
- [68] I. Barrodale and F. D. Roberts, An improved algorithm for discrete L1 linear approximation, *SIAM Journal on Numerical Analysis* **10**, 839 (1973).
- [69] I. Barrodale and F. Roberts, Solution of an overdetermined system of equations in the l1 norm [f4], *Communications of the ACM* **17**, 319 (1974).
- [70] J. Mattsson, H. M. Wyss, A. Fernandez-Nieves, K. Miyazaki, Z. Hu, D. R. Reichman, and D. A. Weitz, Soft colloids make strong glasses, *Nature* **462**, 83 (2009).
- [71] J. Song, Q. Zhang, F. de Quesada, M. H. Rizvi, J. B. Tracy, J. Ilavsky, S. Narayanan, E. Del Gado, R. L. Leheny, N. Holten-Andersen, *et al.*, Microscopic dynamics underlying the stress relaxation of arrested soft materials, *Proceedings of the National Academy of Sciences* **119**, e2201566119 (2022).
- [72] P. J. Green, Iteratively reweighted least squares for maximum likelihood estimation, and some robust and resistant alternatives, *Journal of the Royal Statistical Society: Series B (Methodological)* **46**, 149 (1984).
- [73] W. Y. Wang, A. T. Pearson, M. L. Kutys, C. K. Choi, M. A. Wozniak, B. M. Baker, and C. S. Chen, Extracellular matrix alignment dictates the organization of focal adhesions and directs uniaxial cell migration, *APL bio-engineering* **2**, 046107 (2018).
- [74] Q. Tang, W. Qian, Y. Xu, S. Gopalakrishnan, J. Wang, Y. Lam, and S. Pang, Control of cell migration direction by inducing cell shape asymmetry with patterned topography, *Journal of Biomedical Materials Research Part A* **103**, 2383 (2015).
- [75] Y. Zheng, Q. Fan, C. Z. Eddy, X. Wang, B. Sun, F. Ye, and Y. Jiao, Modeling multicellular dynamics regulated by extracellular-matrix-mediated mechanical communication via active particles with polarized effective attraction, *Physical Review E* **102**, 052409 (2020).
- [76] M. L. Woods, C. Carmona-Fontaine, C. P. Barnes, I. D. Couzin, R. Mayor, and K. M. Page, Directional collective cell migration emerges as a property of cell interactions, *PLoS One* **9**, e104969 (2014).
- [77] J. Zimmermann, B. A. Camley, W.-J. Rappel, and H. Levine, Contact inhibition of locomotion determines cell–cell and cell–substrate forces in tissues, *Proceedings of the National Academy of Sciences* **113**, 2660 (2016).
- [78] J. A. McLennan *et al.*, *Introduction to nonequilibrium statistical mechanics* (Prentice Hall, 1989).
- [79] F. Toschi and M. Sega, *Flowing matter* (Springer Nature, 2019).
- [80] J. Ślęzak and S. Burov, From diffusion in compartmentalized media to non-Gaussian random walks, *Scientific Reports* **11**, 1 (2021).
- [81] D. Selmecki, S. Mosler, P. H. Hagedorn, N. B. Larsen, and H. Flyvbjerg, Cell motility as persistent random motion: theories from experiments, *Biophysical journal* **89**, 912 (2005).
- [82] A. Brugués, E. Anon, V. Conte, J. H. Veldhuis, M. Gupta, J. Colombelli, J. J. Muñoz, G. W. Brodland, B. Ladoux, and X. Trepat, Forces driving epithelial wound healing, *Nature physics* **10**, 683 (2014).
- [83] R. Alert and X. Trepat, Physical models of collective cell migration, *Annual Review of Condensed Matter Physics* **11**, 77 (2020).
- [84] X. Trepat, M. R. Wasserman, T. E. Angelini, E. Millet, D. A. Weitz, J. P. Butler, and J. J. Fredberg, Physical forces during collective cell migration, *Nature physics* **5**, 426 (2009).
- [85] B. Sabass, M. L. Gardel, C. M. Waterman, and U. S. Schwarz, High resolution traction force microscopy based on experimental and computational advances, *Biophys. J.* **94**, 207 (2008).
- [86] F. Giavazzi, D. Brogioli, V. Trappe, T. Bellini, and R. Cerbino, Scattering information obtained by optical microscopy: differential dynamic microscopy and beyond, *Physical Review E* **80**, 031403 (2009).
- [87] J. Nocedal, Updating quasi-newton matrices with limited storage, *Mathematics of computation* **35**, 773 (1980).

APPENDICES

APPENDIX A MAXIMUM LIKELIHOOD ESTIMATOR WITH LAPLACE FLUCTUATION

Here, we discuss the maximum likelihood estimator when the noise fluctuation follows the Laplace dis-

tribution. We use the observations for the x coordinate as an example and the derivation for the y coordinate follows similarly. We denote the observation vector $\mathbf{v}_x = (\mathbf{v}_x^T(1), \mathbf{v}_x^T(2), \dots, \mathbf{v}_x^T(T))^T$ with $\mathbf{v}_x(t) = (v_{1,x}(t), \dots, v_{n_t,x}(t))^T$ for time frame $t = 1, \dots, T$, and assume that the initial velocity $\mathbf{v}_x(0)$ is given. The likelihood function of the parameters $\mathbf{w}_x = (w_x(1), \dots, w_x(T))^T$ and $\boldsymbol{\tau}_x = (\tau_x(1), \dots, \tau_x(T))^T$ can be written as

$$\begin{aligned} & p(\mathbf{v}_x \mid \mathbf{w}_x, \boldsymbol{\tau}_x, \mathbf{v}_x(0)) \\ &= \prod_{t=1}^T p(\mathbf{v}_x(t) \mid \mathbf{v}_x(t-1), w_x(t), \tau_x(t)) \\ &= \prod_{t=1}^T \prod_{i=1}^{n_t} p(v_{i,x}(t) \mid \bar{v}_{i,x}(t-1), w_x(t), \tau_x(t)) \\ &= (\sqrt{2}\tau_x(t))^{-\sum_{i=1}^{n_t} n_t} \exp\left(-\sum_{t=1}^T \sum_{i=1}^{n_t} \frac{\sqrt{2}|e_{i,x}(t)|}{\tau_x(t)}\right), \end{aligned}$$

where the residual of the i th particle at time frame t is defined as $e_{i,x}(t) = v_{i,x}(t) - w_x(t)\bar{v}_{i,x}(t-1)$.

For any time frame t , the maximum likelihood estimator of $w_x(t)$ is equivalent to the least absolute deviation (LAD) regression below:

$$\hat{w}_x(t) = \underset{\tau_x(t), w_x(t)}{\operatorname{argmin}} \sum_{i=1}^{n_t} |v_{i,x}(t) - w_x(t)\bar{v}_{i,x}(t-1)| \quad (\text{A1})$$

Although there is no closed-form solution for the estimator in the LAD regression, fast algorithms, such as the Barrodale and Roberts (BR) algorithm [69], that can transform the LAD regression into a linear programming problem, are available. The BR algorithm is available in standard software platforms. For instance, the package ‘L1pack’ in the Comprehensive R Archive Network

(CRAN) implements the BR algorithm to solve a LAD problem. After obtaining the estimator $\hat{w}_x(t)$, we substitute it into the likelihood function and maximize the profile likelihood to obtain the maximum likelihood estimator of $\tau_x(t)$, which is given in Eq. (7).

APPENDIX B MAXIMUM LIKELIHOOD ESTIMATOR WITH GENERALIZED GAUSSIAN FLUCTUATION

Next, we discuss the maximum likelihood estimator for models with generalized Gaussian fluctuation. To do so, we denote three vectors of parameters \mathbf{w}_x , $\boldsymbol{\alpha}_x$, and $\boldsymbol{\beta}_x$, each having T dimensions. The logarithm of the likelihood function follows

$$\begin{aligned} & \log(p(\mathbf{v}_x \mid \mathbf{w}_x, \boldsymbol{\beta}_x, \boldsymbol{\alpha}_x)) \\ &= \sum_{t=1}^T \left\{ n_t \log \left(\frac{\beta_x(t)}{2\alpha_x(t)\Gamma\left(\frac{1}{\beta_x(t)}\right)} \right) - \sum_{i=1}^{n_t} \left(\frac{|e_{i,x}(t)|}{\alpha_x(t)} \right)^{\beta_x(t)} \right\}, \end{aligned}$$

where $e_{i,x}(t) = v_{i,x}(t) - w_x(t)\bar{v}_{i,x}(t-1)$ and $\Gamma(\cdot)$ denotes the Gamma function, with $w_x(t) \in \mathbb{R}$, $\alpha_x(t) \in \mathbb{R}^+$ and $\beta_x(t) \in \mathbb{R}^+$.

We first differentiate the likelihood function with respect to $\alpha_x(t)$ and set it to zero. For any given $\beta_x(t)$ and $w_x(t)$, the likelihood is maximized when

$$\hat{\alpha}_x(t) = \left(\frac{\beta_x(t)}{n_t} \sum_{i=1}^{n_t} |e_{i,x}(t)|^{\beta_x(t)} \right)^{\frac{1}{\beta_x(t)}}. \quad (\text{A2})$$

After substituting the $\hat{\alpha}_x(t)$ from Eq. (A2) into the log-likelihood function, we obtain the logarithm of the profile likelihood of $(\mathbf{w}_x, \boldsymbol{\beta}_x)$:

$$\log(p(\mathbf{v}_x \mid \mathbf{w}_x, \boldsymbol{\beta}_x, \hat{\boldsymbol{\alpha}}_x)) = \sum_{t=1}^T \left\{ n_t \log \left(\frac{\beta_x(t)}{2\Gamma\left(\frac{1}{\beta_x(t)}\right)} \right) - \frac{n_t}{\beta_x(t)} \log \left(\frac{\beta_x(t)}{n_t} \sum_{i=1}^{n_t} |e_{i,x}(t)|^{\beta_x(t)} \right) - \frac{n_t}{\beta_x(t)} \right\}. \quad (\text{A3})$$

Denoting the logarithm of the profile likelihood by

$\ell(\mathbf{w}_x, \boldsymbol{\beta}_x) = \log(p(\mathbf{v}_x \mid \mathbf{w}_x, \boldsymbol{\beta}_x, \hat{\boldsymbol{\alpha}}_x))$ and differentiating Eq. (A3) with respect to $w_x(t)$ and $\alpha_x(t)$, we then find

$$\frac{\partial \ell(\mathbf{w}_x, \boldsymbol{\beta}_x)}{\partial w_x(t)} = \frac{n_t \sum_{i=1}^{n_t} |e_{i,x}(t)|^{\beta_x(t)-1} \bar{v}_{i,x}(t-1) \operatorname{sgn}(e_{i,x}(t))}{\sum_{i=1}^{n_t} |e_{i,x}(t)|^{\beta_x(t)}}, \quad (\text{A4})$$

$$\frac{\partial \ell(\mathbf{w}_x, \boldsymbol{\beta}_x)}{\partial \beta_x(t)} = \frac{n_t}{\beta_x(t)} + \frac{n_t}{\beta_x^2(t)} \Psi \left(\frac{1}{\beta_x(t)} \right) + \frac{n_t}{\beta_x^2(t)} \log \left(\frac{\beta_x(t)}{n_t} \sum_{i=1}^{n_t} |e_{i,x}(t)|^{\beta_x(t)} \right) - \frac{n_t}{\beta_x(t)} \frac{\sum_{i=1}^{n_t} (|e_{i,x}(t)|^{\beta_x(t)} \log |e_{i,x}(t)|)}{\sum_{i=1}^{n_t} |e_{i,x}(t)|^{\beta_x(t)}}, \quad (\text{A5})$$

where $\Psi(z) = \Gamma'(z)/\Gamma(z)$ stands for the ratio between the derivative of a Gamma function and a Gamma function for any z , and $\text{sgn}(e_{i,x}(t))$ denotes the sign of $e_{i,x}(t) = v_{i,x}(t) - w_x(t)\bar{v}_{i,x}(t-1)$. Thereafter, we iteratively maximize the likelihood function with respect to $w_x(t)$ and $\alpha_x(t)$ using the profile likelihood in Eq. (A3) and closed-form derivative in Eqs. (A4) and (A5) by the low-storage quasi-Newton optimization method (L-BFGS) [87]. Note that, for each t , we only need to iteratively maximize the log profile likelihood with respect to two parameters, making the computational procedure both fast and robust.

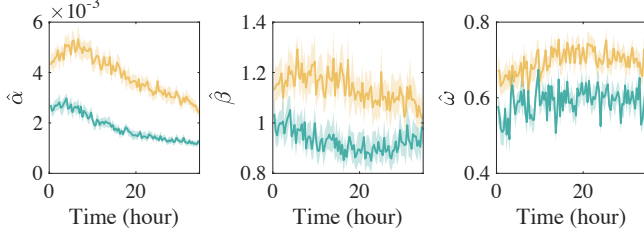


FIG. 9. Parameter estimation with interval (shaded) for a Generalized Gaussian distribution following Eq. (8) along x -direction (yellow), and along y -direction (green).

The maximum likelihood estimators of parameters $\alpha_x(t)$, $\alpha_y(t)$, $\beta_x(t)$, $\beta_y(t)$, $w_x(t)$ and $w_y(t)$ by assuming the fluctuation follows the generalized Gaussian distribution, are shown in Fig. 9. The estimated $\beta_x(t)$ and $\beta_y(t)$ are both close to 1, which means that the fluctuation is closer to the Laplace distribution. In addition, $\beta_y(t)$ is typically smaller than $\beta_x(t)$, as there is more confinement in the y direction because of the substrate-imposed directionality. Furthermore, both $w_x(t)$ and $w_y(t)$ are smaller than 1 for any t , which is consistent with the findings when previously assuming the fluctuation follows the Laplace distribution.

APPENDIX C ADDITIONAL RESULTS ON EXPERIMENTAL DATA

The four new features are used to construct a minimum physics model that can quantitatively capture the progression of the orientational order parameter and velocity distribution, for various experiments with different initial cell densities and liquid-crystalline substrates. The results of several additional experiments are also analyzed to validate the generality of our algorithm (Fig. 12-13). Similar to the main text, we evaluate the models by velocity orientational order parameter and the average absolute deviation of the velocity at each time point.

The experimental setup in Fig. 12 has the same substrate material as the one presented in Fig. 6. Except that at the start of imaging, cell density is higher. During the course of the experiment, the cell density ρ grows from $\rho = 500$ to 650 mm^{-2} . The simulation model with

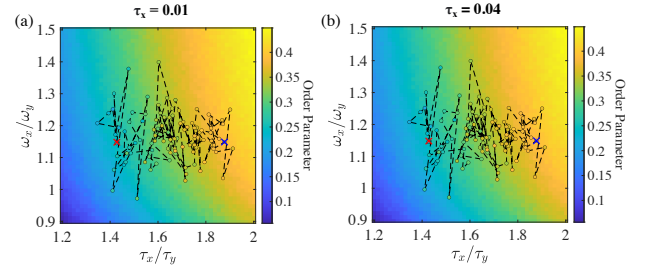


FIG. 10. (a-b) Change of order parameters due to the change of simulation parameters with $\tau_x = 0.01$ in (a) and $\tau_x = 0.04$ in (b), which cover the range of the observed τ 's. $w_x = 0.7$ are assumed for both cases. Red and blue X's denote the beginning and the end of the trajectory.

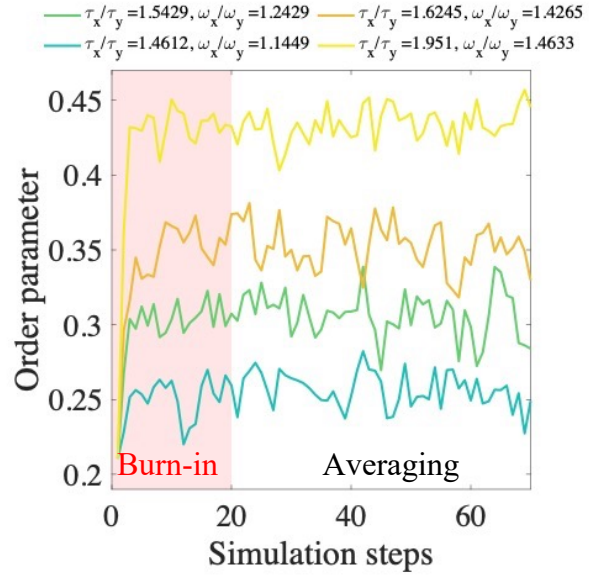


FIG. 11. Plotting several typical simulation progressions, where the first 20 steps are regarded as burn-ins and left out in computing the averages in the phase diagram.

selected features can accurately capture the progression of orientational order parameter and velocity magnitude, shown in upper and lower panels in Fig. 12. Models without all selected features cannot reproduce some of the properties. In particular, if Gaussian fluctuation is used with the other three features (blue curve in panel (a)), the model substantially underestimates the orientational order parameter, while the model with Laplace or GGD fluctuations, shown by blue curves in panel (b) and (c), respectively, reproduce the progression of these parameters reasonably well. Furthermore, all approaches with estimated weights and neighbor resemble containing cells with the same direction velocity capture average absolute deviations of velocities $\bar{\sigma}_x$ and $\bar{\sigma}_y$ reasonably well.

On the other hand, results presented in Fig. 13 are derived from cell movements on an isotropic substrate, during this time, cell density changes from $\rho = 420$ to

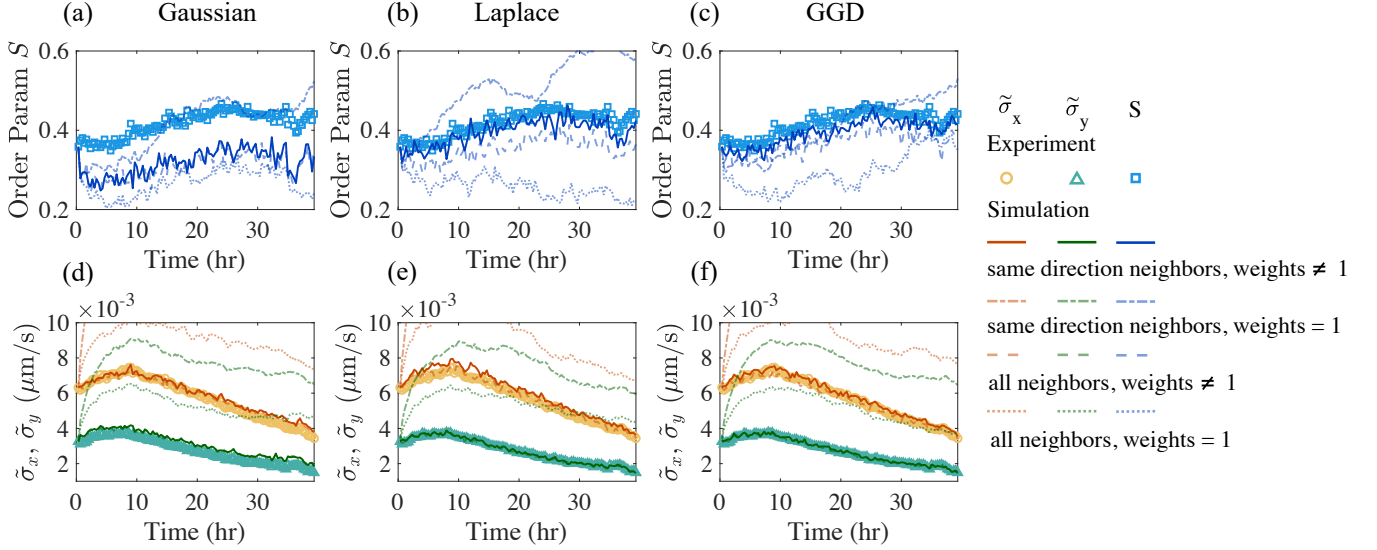


FIG. 12. Reproducing orientational order parameter (a-c) and average absolute deviation of velocities (d-f) from different simulation models at a representative radius $r = 75 \mu\text{m}$ for experiments of cell migrating on a nematic substrate when starting at a higher initial density.

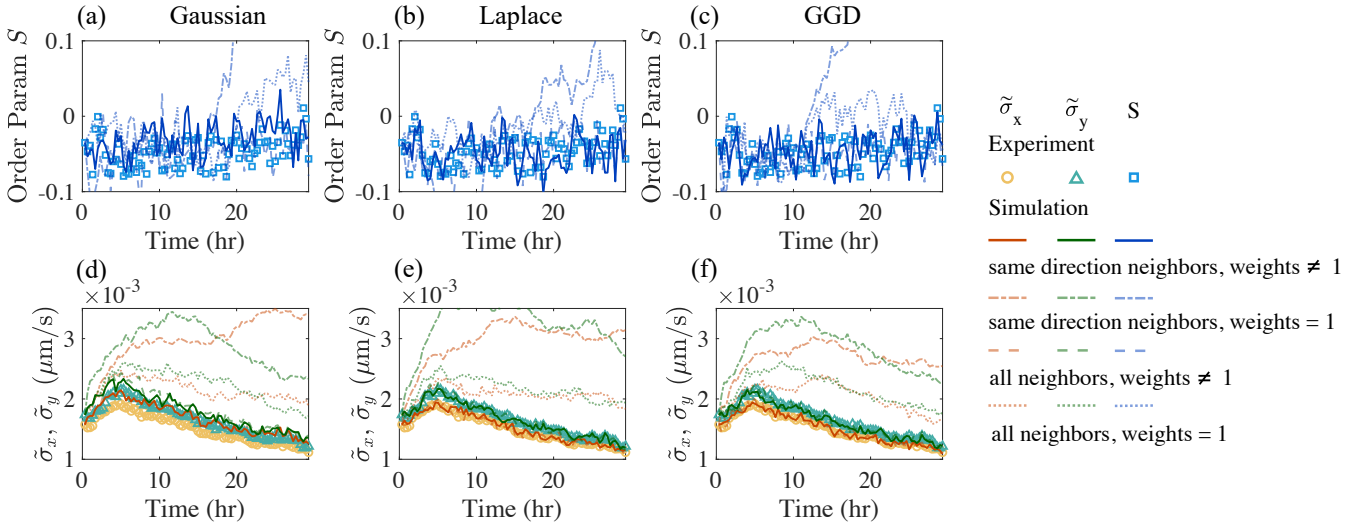


FIG. 13. Reproducing orientational order parameter (a-c) and average absolute deviation of velocities (d-f) with different simulation models at a representative radius $r = 75 \mu\text{m}$ for experiments of cells moving on an isotropic substrate, which do not align, and have isotropic velocity.

470 mm^{-2} . We have observed that, on the isotropic substrate, we reproduce order parameters that are around zero with any type of fluctuations (Fig. 13(a-c)), signaling the lack of order, and the velocity variance is also isotropic (Fig. 13(d-f)). It can be noted that when the cell moves on an isotropic substrate, choices of neigh-

bor, fluctuation distributions, and weights become less important in fitting the order parameter (Fig. 13(a-c)). Nonetheless, the absolute deviation $\tilde{\sigma}_x$ and $\tilde{\sigma}_y$ change over time due to proliferation, and approaches with estimated weights and neighbor resembles of cells with the same direction velocity capture these changes.